

# Numerical study of flow maldistribution and depressurization strategies in a small-scale axial adsorber

Yingshu Liu · Xingang Zheng · Ruifeng Dai

Received: 9 December 2013 / Revised: 5 June 2014 / Accepted: 16 June 2014 / Published online: 22 June 2014  
 © Springer Science+Business Media New York 2014

**Abstract** Flow maldistribution and local high velocity in an axial adsorber is numerically studied to investigate the potential occurrence of sorbent pulverization and uneven utility. A considerable maldistribution induced by the entrance effect and local high velocity caused by rapid gas discharge during depressurization is observed. Three types of gas distributors and different depressurization strategies are then proposed and studied to determine their capabilities to create uniform velocity profiles. Results show that locating the predistributor in the dead zone is critical to flow distribution. The maldistribution factor ( $Mf$ ) can decrease to a minimum of 0.055 when a perforated inlet plenum is used with a conventional distributor. In addition, the internal ring can effectively reduce wall effects. Moreover, both gas expansion and desorption have a significant influence on the evolution of local velocity during depressurization. In this step, local high velocity can possibly exceed incipient fluidization velocity and cause attrition and pulverization of the sorbent. To a certain extent, employing methods to control the depressurization rate is necessary. Applying linear depressurization ( $p = 101,325 - p_{AD}/t_{DP} \times t + p_{AD}$ ) or downward convex conic depressurization ( $p = p_{AD} - \sqrt{(p_{AD} - 101,325)^2/t_{DP} \times t}$ ) can reduce local high velocity, and thus, improve flow conditions.

**Keywords** Mathematical modeling · Adsorption · Packed bed · Transport processes · Flow maldistribution · Distributor

## List of symbols

$a$	Thermal diffusion coefficient, $\text{m}^2 \text{s}^{-1}$
$d_p$	Diameter of adsorbent particle, m
$D_{im}$	Mass dispersion rate, $\text{m}^2 \text{s}^{-1}$
$e_f$	Total fluid energy, $\text{kJ kg}^{-1}$
$e_p$	Total solid medium energy, $\text{kJ kg}^{-1}$
$F$	Momentum source term, $\text{kg m}^{-2} \text{s}^{-2}$
$\Delta H$	Heat of adsorption, $\text{J mol}^{-1}$
$K_i$	Langmuir parameter, $\text{mol kg}^{-1} \text{kPa}^{-1}$
$k_1$	Langmuir temperature dependence constant, $\text{mol kg}^{-1} \text{kPa}^{-1}$
$k_2, k_4$	Langmuir temperature dependence constant, K
$k_3$	Langmuir temperature dependence constant, $\text{kPa}^{-1}$
$k$	Mass transfer rate coefficient, $\text{s}^{-1}$
$k_t$	Turbulent kinetic energy, $\text{m}^2 \text{s}^{-2}$
$k_{eff}$	Effective bed thermal conductivity, $\text{W m}^{-2} \text{K}$
$k_p$	Solid medium thermal conductivity, $\text{W m}^{-2} \text{K}$
$k_f$	Fluid phase thermal conductivity, $\text{W m}^{-2} \text{K}$
$Mf$	Maldistribution factor
$M_i$	Molar weight of component $i$ , $\text{kg mol}^{-1}$
$M_w$	Molar weight of fluid, $\text{kg mol}^{-1}$
$q$	Solid-phase adsorbate concentration, $\text{mol kg}^{-1}$
$q^*$	Adsorbate concentration in equilibrium with gas phase, $\text{mol kg}^{-1}$
$r$	Radial coordinate, m
$R$	Gas constant, $\text{J mol}^{-1} \text{K}^{-1}$ /radius of bed, m
$S_i$	Mass source term of the $i$ th component, $\text{kg m}^{-3} \text{s}^{-1}$
$S_m$	Total mass source term, $\text{kg m}^{-3} \text{s}^{-1}$
$T$	Temperature, K
$u_i$	Velocity in the $i$ direction, $\text{m s}^{-1}$

Y. Liu · X. Zheng (✉)  
 School of Mechanical Engineering, University of Science and Technology, Beijing, China  
 e-mail: zxxg8181@163.com

X. Zheng  
 Institute of Process Engineering, Chinese Academy of Sciences, Beijing, China

R. Dai  
 China ENFI Engineering Corporation, Beijing, China

$u$	Velocity vector, $\text{m s}^{-1}$
$y$	Distance from the adsorber side wall, m
$y_i$	Mass fraction of component $i$
$z$	Axial coordinate, m

### Greek symbols

$\varepsilon$	Porosity of the fixed bed
$\varepsilon_t$	Dissipation rate of turbulence kinetic energy, $\text{m}^2 \text{s}^{-3}$
$\varepsilon_b$	Bulk porosity
$\rho_p$	Density of adsorbent particle, $\text{kg m}^{-3}$
$\rho_f$	Fluid density, $\text{kg m}^{-3}$

### Subscripts

$f$	Fluid
$p$	Particle
$r$	Radial
$i$	Species $i$
*	Equilibrium

## 1 Introduction

Adsorbers are widely used in process industries for gas separation and recovery. An adsorber is typically a vertical axial cylinder, in which sorbent particles are filled into adsorb objectionable species. Sorbents are porous solids with a certain physical strength. Most sorbents are produced artificially, such as zeolite molecular sieves and carbon molecular sieves. During run time, gas is pumped into the adsorber, and the system works alternatively in adsorption and desorption modes. Gas separation is achieved in the alternate loops between the adsorbers. Several researchers (Ruthven 1984; Vortmeyer and Michael 1985; Gouvalias and Markatos 1993; Kwapinski et al. 2004; Todd and Webley 2005) pointed out that axial and radial gas distributions have important roles in the performance of adsorbers. Bad flow distribution can lead to poor product quality, feedstock loss, and excessive energy consumption (Gouvalias and Markatos 1993). In addition, high local velocity can lead to sorbent fluidization, which causes particle attrition and pulverization (Ruthven 1984; Todd and Webley 2005), which, in turn, result in the formation of fragments and fines. Maldistribution and fluidization can decrease the separation performance of an adsorber. Therefore, velocity distribution in the adsorber is one of the key parameters for the reliable and efficient performance of an industrial adsorber.

Meticulous and comprehensive works on velocity distribution in fixed-bed designs have been reported (Bolton et al. 2004; Darakchiev and Dodev 2002; Boysen et al. 2003; Petrova et al. 2003; Hsu et al. 2010). These reports significantly contributed to the development of possible distributors for eliminating maldistribution in adsorbers. However, these studies have been conducted in fixed-bed

reactors, fluidized beds, and high-performance liquid chromatography columns, with several configurations that are different from those of gas adsorbers. The main difference between the structures of an adsorber and a fixed-bed reactor is that in the former, the volumes of two dead zones are required to be smaller than the permissible distribution to obtain highly enriched gas products with high yields; by contrast, minimal dead zone volumes are typically not required in a fixed-bed reactor. Meanwhile, the particles in a fluidized bed are loosely packed for fluidization, thus making it radically different from an adsorber.

Reports on distributor configurations in adsorbers are mostly presented in the form of patents (Hochman and Loboda 1969; Nowobilskij 1994; Nowobilskij et al. 1996; Pan 1999; Smolarek et al. 2002; Mohamed and Bernard 2007). Only a few articles on gas distributors in adsorbers are available in open literature. Gouvalias and Markatos (1993) inferred the use of a gas distributor in an adsorber via a 2D model to study the transfer phenomenon during separation. The model was applied to a single-component system by considering a two-step process, namely, adsorption and regeneration, without studying pressure swing processes such as pressurization and depressurization. In this previous study, a baffle plate distributor was placed at the feed end and a punched tube was placed at the exhaust end. A peak velocity zone and a recirculation zone field were observed at the feed end. The findings of this previous study increase understanding of velocity distribution. However, the credibility of the results would have been improved if the source terms in the total mass conservation equation were considered. Given that sorption involves total mass variations, the lack thereof may cause velocity distribution to deviate partly from the appropriate level.

The transient characteristics of velocity during pressure swing is also worthy to be studied. For example, during depressurization, a large amount of gas can be discharged rapidly from the feed end within a short period. The expelled gas may produce a high velocity in the sorbent layer, which may cause the sorbent to loosen, bounce, and become unstable. However, only a few reports have actually investigated transient velocity during depressurization.

The present study is an extension of our previous work (Zheng et al. 2010), which investigated the transient flow phenomenon in an adsorber. As indicated earlier, velocity maldistribution and high local velocity may affect performances and lead to instability. The objectives of the current study are to investigate different gas distributors that can achieve uniform gas flow in an adsorber and provide an improved depressurization method that can achieve smooth gas flow with gradual variations in velocity and pressure. First, the distribution and evolution of velocities in an adsorber are analyzed. Then different bed-support mechanisms, such as distributors and internal rings, are introduced. Lastly, various depressurization strategies are proposed and studied.

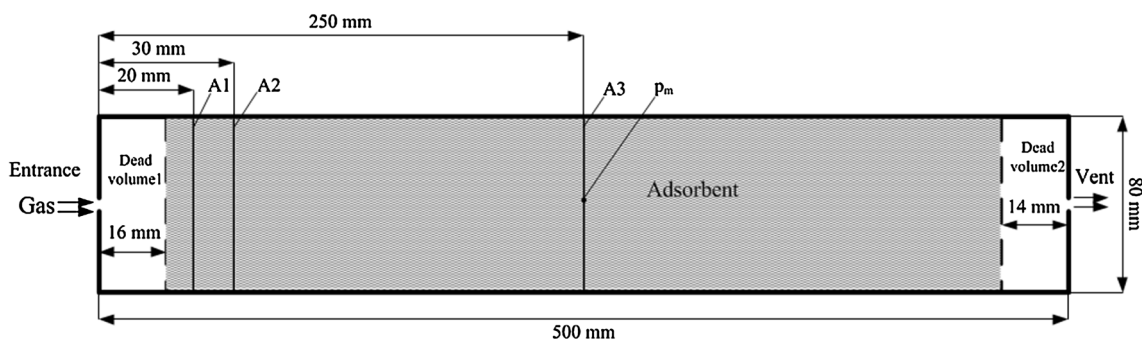


**Fig. 1** Physical model. (Three auxiliary lines from A1 to A3 are added to the figure to represent the three cross sections of different axial heights, which are used to study velocity maldistribution at a

later period. The distance from the cross sections to the inlet are 20, 30, and 250 mm.)

## 2 Theoretical model

### 2.1 Physical model

The physical system of a miniature oxygen generator is illustrated in Fig. 1. The adsorber has a cylindrical axis-symmetric structure with two dead volumes at each end. The length of the adsorber is 500 mm, and its radius is 40 mm. Three auxiliary lines from A1 to A3 are added to the figure to represent the three cross sections of different axial heights, which are used to study velocity maldistribution at a later period. The distances from the cross sections to the inlet are 20, 30, and 250 mm. In this study, a Skarstrom pressure swing adsorption (PSA) cycle comprises four basic steps: pressurization (PR), adsorption (AD), depressurization (DP), and purge (PG). During the cycle, two beds alternately undergo these four operations. Considering the similar adsorption properties of O<sub>2</sub> and Ar in the sorbent, treating air as a mixture of O<sub>2</sub> and N<sub>2</sub> is reasonable to reduce the number of model equations.

### 2.2 Control equations

The governing equations in the porous media are derived via the averaging volume method. Control equations include adsorption equilibrium equations (particle scale), conservation equations (bed scale), and mass transfer rate equations (connections between gas and solid phases).

#### 2.2.1 Mass balance

Mass transfer rate:

$$\frac{\partial q_i}{\partial t} = k_i(q_i^* - q_i). \quad (1)$$

Adsorption equilibrium (Langmuir type, Rege and Yang 1997):

$$q_i^* = \frac{K_i p_i}{1 + \sum_{k=1}^n b_k p_k}, \quad K_i = k_1 \exp\left(\frac{k_2}{T}\right), \quad b_k = k_3 \exp\left(\frac{k_4}{T}\right). \quad (2)$$

Mass balance equation for component  $i$

$$\frac{\partial}{\partial t}(\varepsilon \rho_f y_i) + \nabla \cdot (\varepsilon \rho_f y_i \mathbf{u}) = \nabla \cdot (\varepsilon \rho_f D_{i,m} \nabla y_i) - S_i, \quad (3)$$

$$S_i = (1 - \varepsilon) \rho_p M_i \frac{\partial q_i}{\partial t}, \quad (4)$$

where  $\mathbf{u}$  is the velocity vector,  $\varepsilon$  is the bed porosity,  $\rho_f$  is the density of the gas mixture,  $y_i$  is the mass fraction of component  $i$ ,  $D_{i,m}$  is the mass dispersion rate,  $\rho_p$  is the density of the adsorbent particle,  $M_i$  is the molar weight of component  $i$ , and  $S_i$  is the mass source term of component  $i$  that results from its sorption.

Overall material balance:

$$\frac{\partial \varepsilon \rho_f}{\partial t} + \nabla \cdot (\varepsilon \rho_f \mathbf{u}) = -S_m, \quad (5)$$

$$S_m = \sum_{i=1}^n S_i, \quad (6)$$

where  $S_m$  is the total mass source term that results from bulk sorption.

#### 2.2.2 Momentum balance

The porous media are modeled by adding a momentum source term to standard fluid Navier–Stokes (N–S) equations. The modified N–S equation is written as

$$\frac{\partial}{\partial t}(\rho_f u_i) + \nabla \cdot (\rho_f \mathbf{u} u_i) = \rho_f g - \nabla p + \mu \nabla^2 \mathbf{u} + \frac{\mu}{3} \nabla (\nabla \cdot \mathbf{u}) + \mathbf{F}, \quad (7)$$

where  $\mu$  is the dynamic viscosity of the fluid,  $p$  is the gas pressure, and  $\mathbf{F}$  is the momentum source term. Apart from

the typical momentum sources in the porous media zone, momentum changes in the bed can occur because of gas sorption; hence, an additional source term  $S_m \mathbf{u}$  is added to the momentum equation. Momentum source term  $\mathbf{F}$  is obtained as follows:

$$\mathbf{F} = -\left(\mu \frac{\mathbf{u}}{\alpha} + C_2 \rho_f |\mathbf{u}| \mathbf{u} + S_m \mathbf{u}\right), \quad (8)$$

where  $S_m$  is the total mass source term described in Eq. (6). Coefficients  $\alpha$  and  $C_2$ , which are given by the flow relations in a packed bed developed by Ergun (1952), are expressed as follows:

$$\alpha = \frac{d_p^2 \varepsilon^3}{150(1-\varepsilon)^2}, \quad C_2 = \frac{1.75(1-\varepsilon)}{d_p \varepsilon^3}, \quad (9)$$

where  $\varepsilon$  is the porosity of the bed, and  $d_p$  is the diameter of the adsorbent particle.

Considering the configurations of the distributor, the standard  $k$ – $\varepsilon$  two-equation turbulence model is used to model fluid flow in the dead zone. This model involves two transport equations for turbulence characteristics. The first equation refers to the local kinetic energy of the fluctuating motion  $k_t$ , whereas the second refers to the energy dissipation rate  $\varepsilon_t$

$$\frac{\partial \rho_f k_t}{\partial t} + \nabla \cdot (\rho_f k_t \mathbf{u}) = \nabla \cdot \left[ \left( \mu + \frac{\mu_t}{\sigma_k} \right) \nabla k \right] + G_k - \rho_f \varepsilon_t - Y_M, \quad (10)$$

$$\frac{\partial \rho_f \varepsilon_t}{\partial t} + \nabla \cdot (\rho_f \varepsilon_t \mathbf{u}) = \nabla \cdot \left[ \left( \mu + \frac{\mu_t}{\sigma_{\varepsilon_t}} \right) \nabla \varepsilon_t \right] + C_{1\varepsilon} \frac{\varepsilon_t}{k_t} (G_k + C_{3\varepsilon} G_b) - C_{2\varepsilon} \rho_f \frac{\varepsilon_t^2}{k_t}, \quad (11)$$

where  $\mu_t$  is the eddy viscosity ( $\mu_t = \rho_f C_\mu \frac{k_t^2}{\varepsilon_t}$ ),  $G_k$  represents the generation of turbulence kinetic energy as a result of the mean velocity gradients, and  $Y_M$  represents the contribution of fluctuating dilatation in compressible turbulence to the overall dissipation rate.  $C_{1\varepsilon}$ ,  $C_{2\varepsilon}$ ,  $C_{3\varepsilon}$ , and  $C_\mu$  are constants with values of 1.44, 1.92, 1.92, and 0.09, respectively.  $\sigma_k$  and  $\sigma_{\varepsilon_t}$  are the effective Prandtl numbers for  $k_t$  and  $\varepsilon_t$ , respectively. In the present study,  $\sigma_k = 1.0$  and  $\sigma_{\varepsilon_t} = 1.3$ .

### 2.2.3 Energy balance

For an adiabatic bed with no heat transfer in its surroundings, the overall heat balance can be expressed as

$$\frac{\partial}{\partial t} [\varepsilon \rho_f e_f + (1-\varepsilon) \rho_p e_p] + \nabla \cdot [\mathbf{u} (\rho_f e_f + p)] = \nabla \cdot (k_{eff} \nabla T) - p \nabla \cdot \mathbf{u} + \Phi + S_f^h, \quad (12)$$

$$S_f^h = (1-\varepsilon) \rho_p \sum_i \left( -\Delta H_i \frac{\partial q_i}{\partial t} \right), \quad (13)$$

where  $e_f$  is the total fluid energy,  $e_p$  is the total solid medium energy,  $k_{eff}$  is the effective thermal conductivity of the bed,  $\Phi$  is the dissipation function, and  $\Delta H_i$  is the heat of adsorption.

The effective thermal conductivity is expressed as

$$k_{eff} = \varepsilon k_f + (1-\varepsilon) k_p, \quad (14)$$

where  $k_f$  is the thermal conductivity of the fluid phase, and  $k_p$  is that of the solid medium.

The equation of state is

$$\rho_f = \frac{P}{\frac{R}{M_w} T}, \quad (15)$$

where  $R$  is the gas constant, and  $M_w$  is the molar weight of the fluid.

### 2.2.4 Porosity

Considering the effects of the adsorber walls, the void fraction exhibits some form of distribution in the radial direction (Roblee et al. 1958; Benenati and Brosilow 1962). The following model for the sphere sorbent is reported to effectively represent the radial void fraction profile (Nield and Bejan 2006):

$$\varepsilon = \varepsilon_b [1 + 1.4 \exp(-5y/d_p)], \quad (16)$$

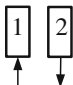
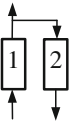
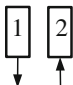
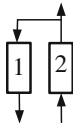
where  $\varepsilon_b$  is the bulk porosity,  $y$  is the distance from the adsorber side wall, and  $d_p$  is the diameter of the adsorbent particle.

### 2.3 Solving method

The aforementioned equations are numerically solved by using the computational fluid dynamics (CFD) software FLUENT (ANSYS, Inc. PA, USA), whereas the pressure–velocity coupling problem in the momentum equations is solved by using the coupled algorithm. The solving process and model parameters were described in a previous study (Zheng et al. 2010). After verifying grid independence, the total grid is determined to be approximately 11,730 when no distributor is considered, and approximately 120,814–159,236 when different distributors are considered.

The cycle sequence and the main parameters are shown in Tables 1 and 2, respectively. Conventional depressurization time  $\tau_{DP}$  is a dependent variable that is determined from the other process variables, and is generally considerably shorter than the step time (9 s). When bed pressure decreases to a low operating pressure (101,325 Pa), the DP step is considered to be complete. As shown in Table 2, mass flow rate is set based on the displacement of the

**Table 1** Cycle sequence

Item	Step 1	Step 2	Step 3	Step 4
Schematic				
Duration (s)	9, $\tau_{DP}$	5	$\tau_{DP}$ , 9	5

**Table 2** Main model parameters

	LiX zeolite
Adsorbent	
Particle density, $\rho_p$ (kg m <sup>-3</sup> )	1,035
Radius, $r_p$ (mm)	0.8
Adsorption bed	
Height of dead volume 1, $h_1$ (mm)	16
Height of dead volume 2, $h_2$ (mm)	14
Radius of entrance tube, $r_{in}$ (mm)	4
Radius of vent tube, $r_{out}$ (mm)	4
Bulk porosity, $\varepsilon_\infty$	0.4
Feed composition	21 % O <sub>2</sub> , 79 % N <sub>2</sub>
Feed mass flow rate (kg s <sup>-1</sup> )	0.00224

compressor (ZW-700A), which has an average mass flow rate of approximately 0.00224 kg/s (104 L/min).

User-defined scalars (UDS) and user-defined functions, which allow the mass transfer rate equations and the source terms to be programmed, are applied to implement adsorption. One treatment approach for the source terms in the porous media is described as follows. The partial derivative in the mass transfer rate [Eq. (1)] is approximately replaced by the finite difference and then transformed into Eq. (17). Adsorption loading  $q_n$ , which is obtained from Eq. (17), can then be described as Eq. (18). The value of  $q_n$  is stored in the UDS. The term  $t_n - t_{n-1}$  denotes the time step, which can be obtained by using Macro RP\_Get\_Real (“physical-time-step”).

$$\frac{\partial q_n}{\partial t} = \frac{q_n - q_{n-1}}{t_n - t_{n-1}} = k_i(q_n^* - q_{n-1}) \quad (17)$$

$$q_n = q_{n-1} + k(q_n^* - q_{n-1})(t_n - t_{n-1}). \quad (18)$$

## 2.4 Model validation

The prediction accuracy of the model with regard to cycle behavior has been verified by comparing its result with that of the experiment and by referring to a previous work (Zheng et al. 2010). Velocity distribution within the sorbent zone is difficult to measure because related studies are rare in

literature. Considering the lack of suitable measurements for interparticle velocity, the performance of velocity distribution is not verified in the present study. In the follow-up studies, the performance of the model has been indirectly validated through air breakthrough experiments. In these experiments, pressure, axial and radial multiple-point temperatures, as well as vent gas concentration, are measured. Transient adsorber pressure, vent oxygen concentration trends, and inner temperatures can be favorably predicted. A subsequent paper that is currently being written provides details of the comparisons between the results of the model and the experiments. Furthermore, a CFD model is comparable with the model setup, and CFD can be used as a design tool.

## 3 Results and discussion

### 3.1 Velocity distribution

According to a previous study (Zheng et al. 2010), given the redistribution effects of the porous media layer, the sorbent itself can eliminate the existing non-uniform velocity at the feed end as gas passes through the bed, thus making the velocity uniform in a short distance. However, velocity maldistribution at the edge of the porous media remains after pressurization (Fig. 2). The axial velocity that passes through line A1 (20 mm away from the inlet) forms a W shape, which is uneven, and peak velocities are observed in the core and near-wall regions.

When gas velocity is sufficiently high, fluidization may occur. To prevent attrition resulting from the movement of particles within the bed, limiting the allowable upflow velocity to approximately less than 80 % of the minimum fluidization velocity is normal (Ruthven 1984), and can be expressed as follows:

$$v_{\max} = 0.8v_{mf} \approx 6 \times 10^{-4} g \frac{(2R_p)^2}{\mu} (\rho_p - \rho_f), \quad (19)$$

where  $v_{mf}$  is the minimum fluidization velocity,  $\rho_p$  is the density of the adsorbent particle,  $\rho_f$  is the fluid density,  $\mu$  is the dynamic viscosity, and  $R_p$  is the particle radius.

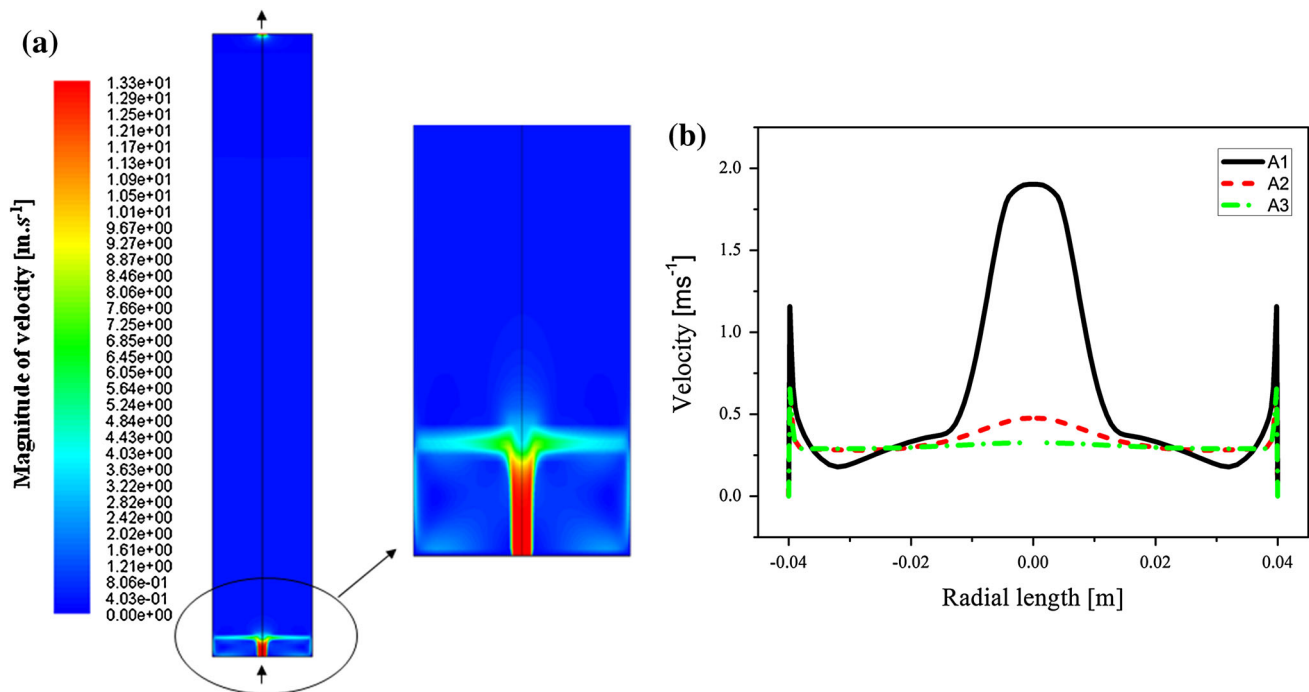


**Fig. 2** Velocity distribution during the end of the PR step: **a** contours and **b** radial profile

For the sorbent with a particle density of  $1035 \text{ kg/m}^3$  and a particle diameter of  $1.6 \text{ mm}$ , the maximum allowable interstitial velocity for upflow through the bed is set to approximately  $0.85 \text{ m/s}$  [Eq. (19)]. For downflow, Ruthven (1984) pointed out that the tolerable fluidization velocity may be approximately 1.8 times the minimum fluidization velocity, which is approximately  $1.52 \text{ m/s}$ . However, operating a PSA cycle at or above the incipient fluidization point can be disastrous for the adsorbent because rapid attrition of pellets can occur (Todd and Webley 2005). The velocity in the core and near-wall regions exceeds the fluidization velocity (Fig. 2b), thus indicating that attrition and pulverization of the sorbent occur. The central high velocity is influenced by the entrance effect, whereas the high near-wall velocity is caused by wall effects that result from radial porosity variation [Eq. (16)]. Although the length of the existing maldistribution region is narrow compared with the bed height, local attrition and fluidization frequently indicate the beginning of performance deterioration. Moreover, wall effects typically make the breakthrough in near-wall regions faster than that in the core of the adsorber, thus indicating that the occurrence of such effects reduces bed utilization (Kwapinski 2009; Zheng et al. 2010). Hence, employing methods to eliminate maldistribution in the core and near-wall regions is necessary.

Figures 3a–d show the evolution and distribution of axial velocity during a complete PSA cycle. Axial velocity significantly changes with time in each step. During the AD step (Fig. 3b), the velocity within the sorbent zone forms a

staircase shape, and the slope of the velocity rapidly changes as a result of bulk sorption. The terraced regions correspond to the mass transfer zone, wherein most of the nitrogen is adsorbed and the oxygen is purified. The velocity slightly changes before and after reaching the mass transfer zone, whereas in the other three steps, the velocity within the sorbent zone varies approximately linearly. During the PR step (Fig. 3a), axial velocity is gradually reduced over time because of the volumetric flow decrease caused by elevatory pressure. During the PG step (Fig. 3d), axial velocity initially increases and then decreases as the purging gas propagates in the bed and replaces the adsorbed gas. The main difference of the DP step (Fig. 3c) is that axial velocity is fairly high in this step compared with those in the other three steps, and is also considerably greater than fluidization velocity. The gas discharged in this step blows the sorbent rapidly, thus loosening it. This process results in attrition, which is also a potential factor for bed instability. Applying depressurization strategies to research, regulate, and control maldistribution and fluidization is necessary. The corresponding methods to reduce maldistribution and fluidization are discussed in the following sections.

### 3.2 Internal distributor design and simulation of the adsorber

Flow non-uniformity at the feed end of an adsorber is one of the most important factors that leads to the low utilization rate of the sorbent; this factor also explains why



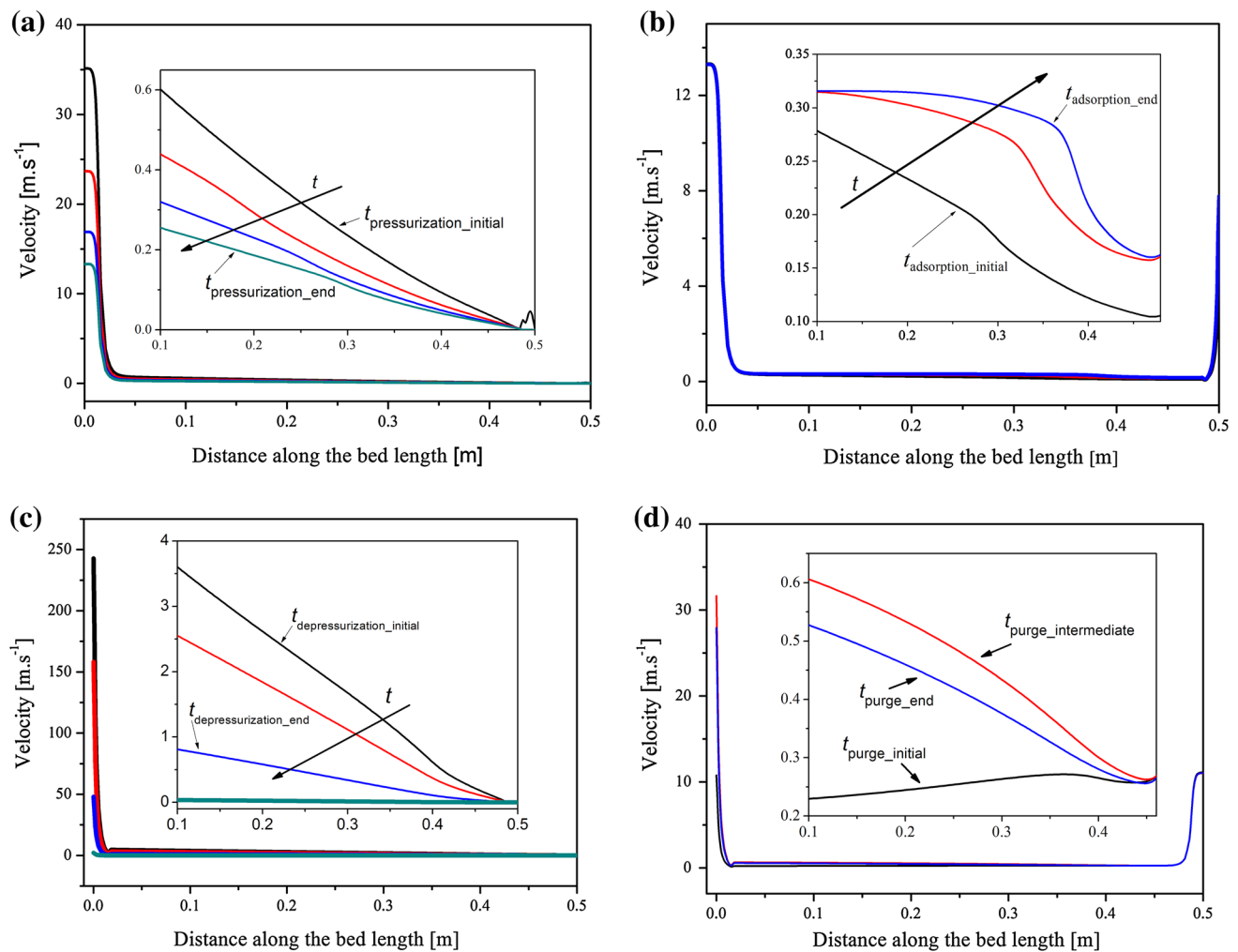


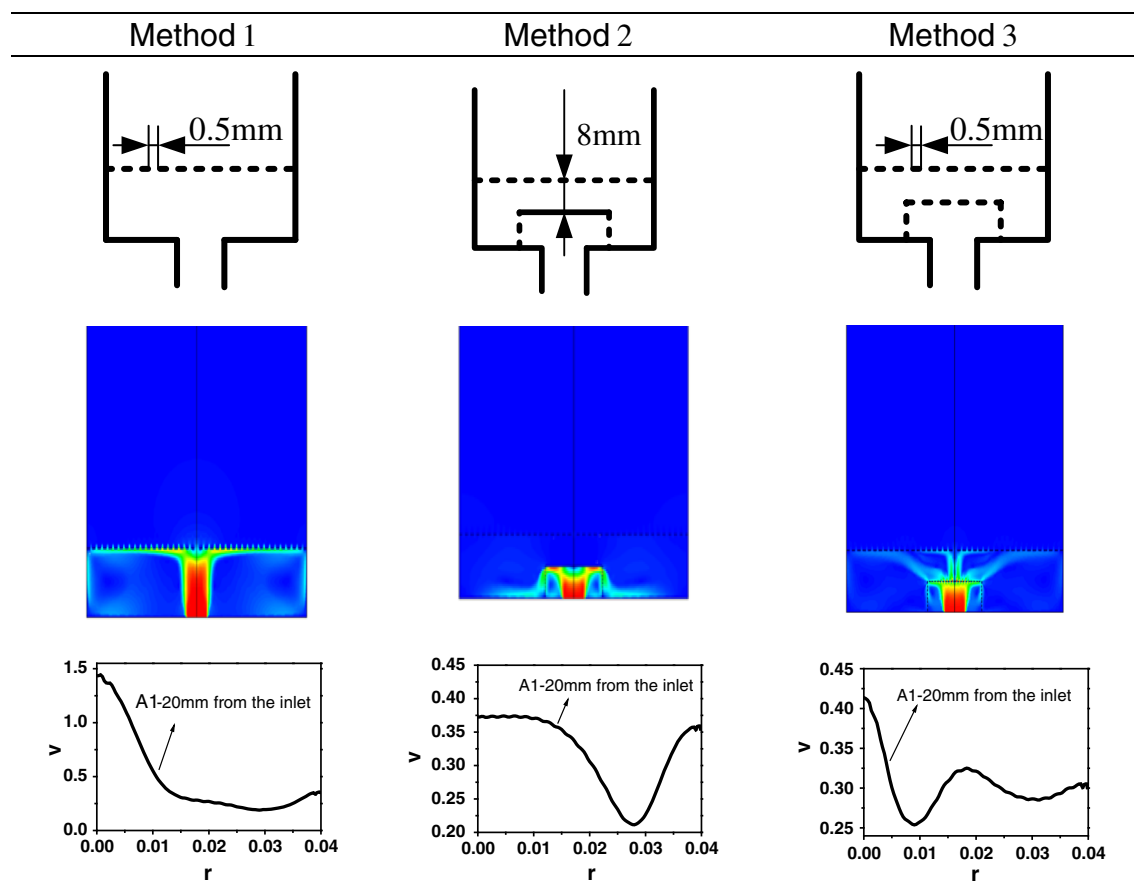
**Fig. 3** Axial velocity distribution during the: **a** PR step ( $\tau_{PR} = 9$  s,  $\Delta t = 3$  s),  $\Delta t$  indicates the time interval between adjacent curves; **b** AD step ( $\tau_{AD} = 5$  s,  $\Delta t = 2.5$  s); **c** DP step ( $\tau_{DP} = 2$  s,  $\Delta t = 0.7$  s), and **d** PG step ( $\tau_{PG} = 5$  s,  $\Delta t = 2.5$  s)

determining the optimum design for the structure of a flow distributor has become increasingly important. To investigate the performances of different distributors, three kinds of distributors, called methods 1, 2, and 3, have been studied. The velocity contours are shown in Table 3. Wall effects are disregarded for simplicity, and will be reconsidered in the follow-up work.

As shown in Table 3, method 1 is a conventional and simple method, in which pressurized gas enters the adsorber through numerous holes via a plate known as the distributor plate, which is located at the bottom of the sorption bed. In this plate, holes with diameters of 0.5 mm are uniformly distributed across the space. The percentage open rate of this distributor is approximately 50 %. Methods 2 and 3 introduce a cylindrical perforated inlet plenum as the predistributor at the feed end. The inlet plenum in method 2 is covered with a solid top plate, whereas that in method 3 is covered with a perforated top

plate. The corresponding simulation results of the different methods are also shown in Table 1.

The result for method 1 shows that a larger than average flow directly follows the short path from the inlet to the bottom of the adsorbent layer, thus resulting in the indicated high gas flow velocity in that region. When gas flows through the distributor plate, a non-uniform flow also maintains a high velocity head. Therefore, simply placing a perforated plate to reduce maldistribution is insufficient. In method 2, gas velocity at the inlet plenum is reduced, and gas is forced to exit the side of the plenum cylinder. This arrangement does not force gas flow from the inlet plenum to move upward, and a recirculating concentrated gas velocity distribution is achieved. This type of gas recirculation was also observed and depicted by Gouvalias and Markatos (1993). This recirculation results in low velocities near the radial location of 0.03 m at the edge of the adsorbent layer. The inlet plenum of method 3 has a

**Table 3** Three kinds of gas distributors and their corresponding performances (Color figure online)

perforated top plate that facilitates gas flow to the center region of the vessel head. The plenum in method 3 provides a low-resistance gas-flow path upward and outward to the dead volume, thus achieving a relatively uniform gas velocity distribution across the bottom of the adsorbent bed. The upward flow partly offsets the side recirculation that occurs in method 2. Therefore, the upper plate in the plenum controls upward gas flow.

The non-uniform velocity distribution over the cross section can be characterized by the maldistribution factor ( $Mf$ ), which is a quantity that integrates the surface and its corresponding velocity (Darakhchiev and Dodev 2002). The coefficient of variation,  $Mf$ , is defined as

$$Mf = \sqrt{\frac{1}{F_0} \int_0^{F_0} \left( \frac{w_i - \bar{w}}{\bar{w}} \right)^2 dF}, \quad (20)$$

where  $F_0$  is the total bed cross section;  $w_i$  is the flow velocity in point  $i$ ; and  $\bar{w}$  is the overall mean velocity, which is further defined as

$$\bar{w} = \frac{1}{F_0} \int_0^{F_0} w_i dF. \quad (21)$$

When the value of  $Mf$  is large, the maldistribution is considerable. In case of a uniform distribution, the value of this factor is zero. In the present study,  $Mf$  along line A1 is calculated under different conditions (Fig. 4).

Flow maldistributions are significant under the conditions of no distributor and method 1 (Fig. 4). Wall effects contribute approximately 0.07 to  $Mf$ , which is obtained from the comparison between the two conditions without a distributor. Meanwhile, method 3 results in significantly low  $Mf$ .  $Mf$  decreases from 0.58 for a conventional distributor to 0.055 for the improved distributors. Compared with method 3, method 2 provided a slightly larger  $Mf$ . The difference between methods 2 and 3 is mainly attributed to the blocking of the solid plate in the central gas path, which causes the previously mentioned gas recirculation. This condition generally conforms to the velocity distribution



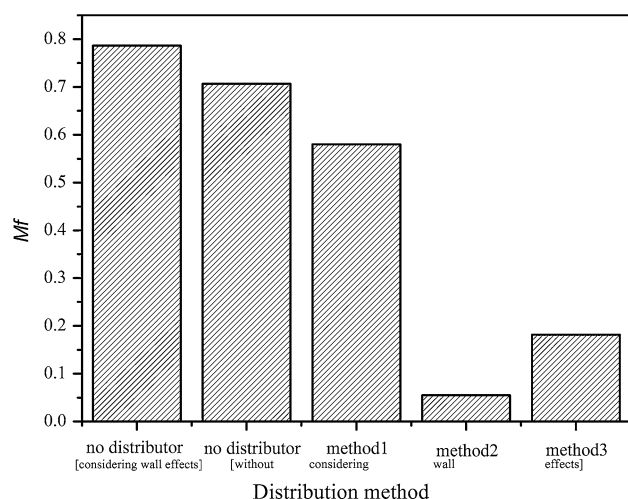


**Fig. 4** Maldistribution factor ( $Mf$ ) of different distributors along line A1

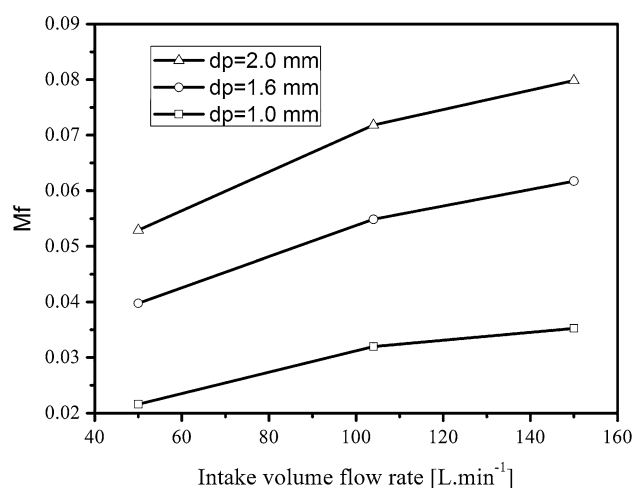


**Fig. 5**  $Mf$  of different sorbent diameter under method 2 along line A1

that enters the adsorbent bed, as shown in the head section configuration in Table 3.

Figure 5 shows the maldistribution of method 3 under different sorbent diameters and intake volume flow rates. Maldistribution slightly increases with the increase in sorbent diameter and volume flow rate. However,  $Mf$  is only 0.08 even under the following conditions: 150 L/min gas flow rate and 2 mm sorbent diameter.

The results from the aforementioned analysis indicate that the gas jet at the entrance significantly affects gas distribution. Removing the entrance effect is difficult by depending solely on the distributor plate. Locating an appropriate predistributor in the dead zone is critical to flow distribution. The primary functions of the perforated inlet plenum are: (1) to direct incoming gas flow, which beneficially utilizes pressure drop through the perforated

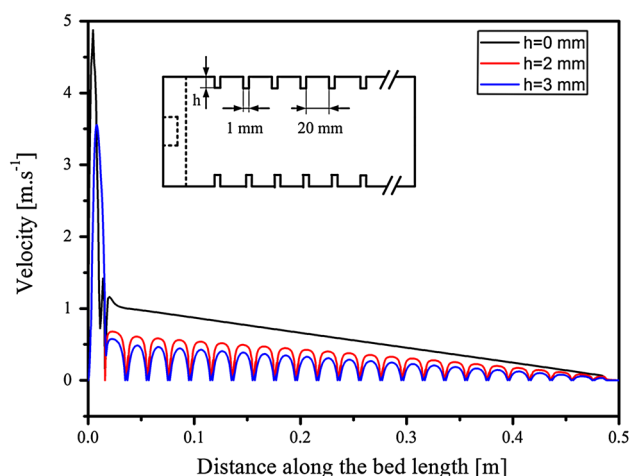


**Fig. 6** Axial velocity in the near-wall regions with and without an internal ring

tube to force gas flow to the outer region of the adsorber; and (2) to reduce the velocity of the gas flow that is entering the bed of the adsorbent material. The perforated inlet plenum in method 3 is the recommended configuration. The conclusions obtained from method 3 can serve as guidelines for the optimum design of flow distributors in the industry.

### 3.3 Influence of internal rings on reducing wall effects

The influence of internal rings on reducing wall effects is briefly studied. Figure 6 shows the velocity profile of different ring heights along an axial curve, with the axial position located 0.2 mm away from the adsorber wall. A damping with a saw tooth profile is formed (Fig. 6), with the number of saw teeth being the same as the number of rings. The width of the saw tooth is equal to the distance between adjacent rings. The height of the saw tooth is reduced with increasing thickness of the ring. Increasing the height of the internal ring may help reduce wall effects. For example, when the height of the ring is 3 mm, the velocity is approximately half of the original velocity. Therefore, the influence of internal rings on reducing wall effects is apparent. Consequently, internal rings further facilitate uniform gas flow gas across near-wall regions.

### 3.4 Effects of different depressurization strategies on velocity evolution

Gas is generally freely and directly discharged to the atmosphere without any restriction during depressurization. This process is called the free depressurization process (F\_DP) in this study. In F\_DP, velocity and pressure significantly change, thus possibly intensifying sorbent

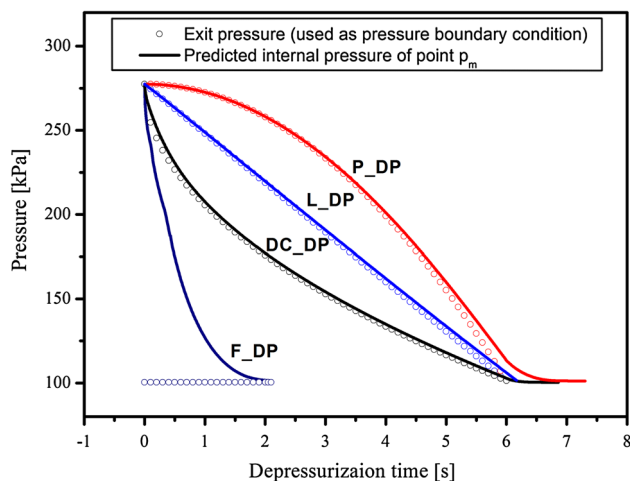


**Fig. 7** Pressure trends with time under different depressurization methods

fluidization and attrition. Improving the mechanical strength of the sorbent considerably reduces pulverization degree; however, taking appropriate depressurization measures is also an important auxiliary method for this process. Three other depressurization methods are used to adjust the evolution of velocity over time, and their corresponding expressions are described in Eqs. (22)–(24). The difference between F\_DP and the proposed depressurization methods is notable in terms of exit pressure. The exit pressure of F\_DP is a constant variable that equals to 101,325 Pa, whereas the exit pressure of the proposed depressurization methods is a known independent variable that changes with time, and thus, these auxiliary methods affect and improve interparticle gas pressure and velocity. The aforementioned three formulas are used as pressure boundary conditions to simulate depressurization. The exit pressure profiles with time, as well as the predicted internal pressure profiles, are illustrated in Fig. 7. The predicted pressure evolution of F\_DP takes approximately 2 s to complete depressurization. By contrast, the depressurization time ( $t_{DP}$ ) adopted in the aforementioned three equations is intentionally set to 6 s, which is slightly shorter than the duration of the parallel PR step (9 s). Another significant difference is noted in terms of profiles. The F\_DP profile exhibits sharp pressure slop, whereas those of the proposed methods gradually vary under different concave–convex trends.

Linear depressurization (L\_DP) rate:

$$p = a \times t + b, \quad a = \frac{101,325 - p_{AD}}{t_{DP}}, \quad b = p_{AD}. \quad (22)$$

Parabolic depressurization (P\_DP) rate:

$$p = a' \times t^2 + b', \quad a' = \frac{101,325 - p_{AD}}{t_{DP}^2}, \quad b' = p_{AD}. \quad (23)$$

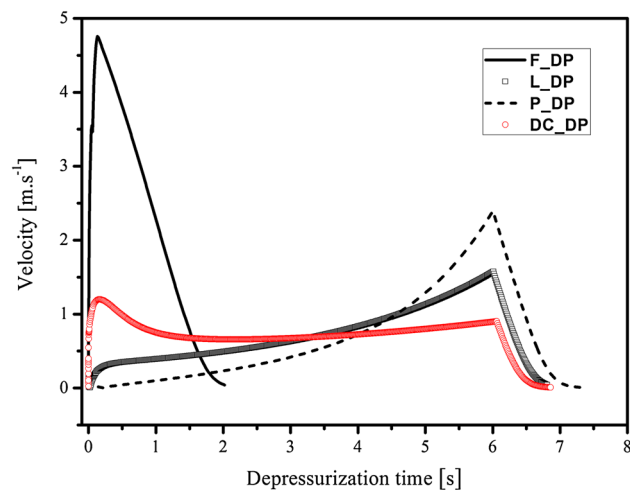


**Fig. 8** The velocity evolution of middle point ( $p_m$ ) over time under differential depressurization methods

Downward convex conic depressurization (DC\_DP) rate:

$$p = b'' - \sqrt{a'' \times t}, \quad a'' = \frac{(p_{AD} - 101,325)^2}{t_{DP}^2}, \quad b'' = p_{AD}. \quad (24)$$

The velocity evolution of the middle point ( $p_m$ ) under different depressurization strategies is shown in Fig. 8. The F\_DP method exhibits a spire-shaped velocity profile with a dramatic change within a short period and a corresponding peak value of approximately 4.8 m/s. Compared with the F\_DP method, velocity trends significantly change in the proposed methods. The velocities in L\_DP and P\_DP slowly increase until a peak value achieved. The initial velocity in DC\_DP rapidly increases to a relatively large value and then slowly declines from a peak value until it becomes nearly flat. Velocity discontinuity points are observed in the proposed methods (Fig. 8), wherein pressure decreases to a low operating value (101,325 Pa). This phenomenon can be attributed to the effluent gas being released from two different origins (one corresponding to compression and the other corresponding to gas desorption from the solid phase) during gas depressurization. The relationships are described as follows:

$$q_{discharge} = q_{compression} + q_{desorption}, \quad (25)$$

$$q_{compression} = F\left(\frac{\partial p}{\partial t}, \frac{\partial T}{\partial t}\right), \quad (26)$$

$$q_{desorption} = F\left(\frac{\partial q^*}{\partial t}\right) = F\left(\frac{\partial q^*}{\partial p} \frac{\partial p}{\partial t}, \frac{\partial q^*}{\partial T} \frac{\partial T}{\partial t}\right). \quad (27)$$

The aforementioned equations show how the discharge rate is affected by compression and desorption. Under certain depressurization rates, both compression and desorption have their own functions in dischargement,

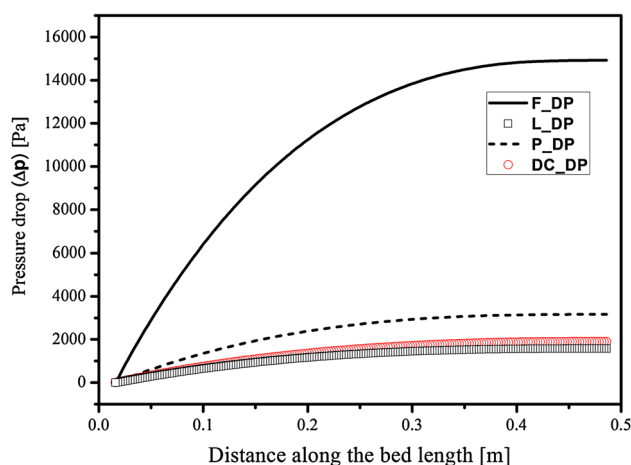


**Fig. 9** Pressure decrease in the adsorber under differential depressurization methods

during which the pressure derivative ( $\frac{\partial p}{\partial t}$ ) directly affects the compression term  $q_{compression}$  and indirectly affects the sorption term  $q_{desorption}$ . The slope of the Langmuir-type isotherm gradually decreases with increasing pressure at a constant temperature; hence, adsorption loading  $q^*$  is less affected by high pressure than by low pressure.

The DC\_DP process (Figs. 7, 8) is used to explain how velocity evolves with time. High velocity during the initial moment (Fig. 8) is caused by the rapid depressurization rate (Fig. 7). The subsequent flat velocity results from the DC\_DP curve, and the Langmuir-type isotherm is nearly symmetrical in the  $x$  axis. These two factors have a balancing effect on the discharge.

Velocity begins to decrease after the discontinuity point because of the pressure lag (Fig. 7) that occurs between the interparticles and the outlet, wherein outlet pressure varies according to Eq. (24), whereas interparticle pressure slowly responds because of the volume effect and nozzle resistance. In addition, various depressurization methods provide different local velocities at the discontinuity point.

Figure 9 shows the pressure decrease along the bed length with the time that corresponds to the emergence of peak velocities shown in Fig. 8. The pressure decrease in F\_DP is significantly larger than those in the proposed methods. This considerable pressure drop is highly conducive to particle attrition. Meanwhile, the L\_DP and DC\_DP methods can effectively reduce pressure decrease.

As discussed earlier, interparticle velocity, with regions below fluidization velocity, significantly changes depending on the depressurization methods used. Such capability offers significant advantages in achieving a smooth gas flow with gradual variations in velocity and pressure. The L\_DP and DC\_DP methods are recommended as the best choices for regulating and controlling transient velocity during depressurization. These methods are implemented

by using a feedback system to regulate valve opening, and thus, ensure that outlet pressure can be adjusted accordingly via Eqs. (24) or (22).

## 4 Conclusion

Understanding and controlling the formation of velocity inside an adsorber by optimizing distributor designs and depressurization methods are important to improve the performance of adsorbers. In this study, flow distribution is studied numerically by considering several factors to investigate the potential cause of sorbent pulverization and uneven utility. A significant maldistribution induced by the entrance effect at the feed end is observed. Then, the performances of three types of distributors are investigated and evaluated. The conventional distributor plate still results in a large maldistribution, whereas the configurations with a perforated inlet plenum can effectively improve flow performance. Meanwhile,  $Mf$  decreases from 0.58 to a minimum of 0.055. Gas recirculation is observed in the perforated inlet plenum with a solid plate, which provides an  $Mf$  of 0.18. In addition, internal rings can significantly reduce wall effects. Therefore, integrating internal rings into method 3 (perforated inlet plenum with a perforated plate) is the recommended configuration for an axial adsorber design. However, the performances of the distributors are also affected by many other structure parameters, such as spacing, size, placement, open area percentage, hole diameter, relative distance between the distributor and the predistributor, as well as the shape and size of the predistributor. Hence, further in-depth studies are required.

The transient flow phenomenon during depressurization is also studied. Local velocity is high during free depressurization, and most values exceed incipient fluidization velocity, thus implying that attrition and pulverization of the sorbent occur. During depressurization, the evolution of local velocity is affected by the expansion and desorption of gas. Therefore, different depressurization strategies are proposed and investigated as auxiliary improvement methods. These strategies provide various velocity evolutions. Among these, L\_DP ( $p = 101,325 - p_{AD}/t_{DP} \times t + p_{AD}$ ) and DC\_DP ( $p = p_{AD} - \sqrt{(p_{AD} - 101,325)^2/t_{DP} \times t}$ ) can effectively reduce local velocity, and thus, improve flow conditions. A depressurization method can be implemented by using a feedback system to regulate valve opening, and thus, ensure that outlet pressure can be changed accordingly.

**Acknowledgments** The authors acknowledge the financial support provided by the 863 Project (No. 2009AA063201), Ministry of Science and Technology, People's Republic of China. The authors also thank the anonymous reviewers and the editor for their valuable comments.

## References

- Benenati, R.F., Brosilow, C.B.: Void fraction distribution in beds of spheres. *AIChE J.* **8**(3), 359–361 (1962)
- Bolton, G.T., Hooper, C.W., Mann, R., Stitt, E.H.: Flow distribution and velocity measurement in a radial flow fixed bed reactor using electrical resistance tomography. *Chem. Eng. Sci.* **59**(10), 1989–1997 (2004)
- Boysen, H., Wozny, G., Laiblin, T., Arlt, W.: CFD simulation of preparative HPLC columns with consideration of nonlinear isotherms. *Chem. Eng. Technol.* **26**(6), 651–655 (2003)
- Darakchiev, R., Dodev, C.: Gas flow distribution in packed columns. *Chem. Eng. Process.* **41**(5), 385–393 (2002)
- Ergun, S.: Fluid flow through packed columns. *Chem. Eng. Prog.* **48**(2), 89–94 (1952)
- Gouvalias, G.S., Markatos, N.C.: Mathematical modeling of heat and mass transfer in packed-bed adsorbers/regenerators. *AIChE J.* **39**(11), 1799–1809 (1993)
- Hochman, J.M., Loboda, W.J.: Fluid flow distributor. U.S Patent, 3479146, 1969
- Hsu, C.J., Hsiau, S.S., Chen, Y.S., Smid, J.: Investigation of the gas inlet velocity distribution in a fixed granular bed filter. *Adv. Powder Technol.* **21**(6), 614–622 (2010)
- Kwapinski, W.: Combined wall and thermal effects during non-isothermal packed bed adsorption. *Chem. Eng. J.* **152**(1), 271–276 (2009)
- Kwapinski, W., Winterberg, M., Tsotsas, E., Mewes, D.: Modeling of the wall effect in packed bed adsorption. *Chem. Eng. Technol.* **27**(11), 1179–1186 (2004)
- Mohamed, S.A.B., Bernard, T.N., Dariush, H.Z.: Flow distributor for PSA vessel. U.S Patent, 7166151 B2, 2007
- Nield, D.A., Bejan, A.: Convection in porous media. Springer-Verlag, New York (2006)
- Nowobilskij, J.J.: Perforated plate fluid distributor and its associated fixed bed vessel. U.S Patent, 5298226, 1994
- Nowobilskij, J.J., Gottzmann, C.F., Notaro, F.: Adsorption flow distribution. U.S Patent, 5538544, 1996
- Pan, C.Y.: Spiral fixed-bed module for adsorber and catalytic reactor. U.S Patent 5,916,531, 1999
- Petrova, T., Semkov, K., Dodev, C.: Mathematical modeling of gas distribution in packed columns. *Chem. Eng. Process.* **42**(11), 931–937 (2003)
- Rege, S.U., Yang, R.T.: Limits for separation by adsorption with LiX zeolite. *Ind. Eng. Chem. Res.* **36**(12), 5358–5865 (1997)
- Roblee, L.H.S., Baird, R.M., Tierney, J.M.: Radial porosity variations in packed beds. *AIChE J.* **4**(4), 460–464 (1958)
- Ruthven, D.M.: Principles of adsorption and adsorption processes, 1st edn. Wiley, New York (1984)
- Smolarek, J., Nowobilskij, J.J., Ackley, M.W.: Bed restraint for an adsorber. U.S Patent, 6334889 B1, 2002
- Todd, R.S., Webley, P.A.: Pressure drop in packed bed under nonadsorbing and adsorbing conditions. *Ind. Eng. Chem. Res.* **44**(18), 7234–7241 (2005)
- Vortmeyer, D., Michael, K.: The effect of non-uniform flow distribution on concentration profiles and breakthrough curves of fixed bed adsorbers. *Chem. Eng. Sci.* **40**(11), 2135–2138 (1985)
- Zheng, X.G., Liu, Y.S., Liu, W.H.: Two-dimensional modeling of the transport phenomena in the adsorber during pressure swing adsorption process. *Ind. Eng. Chem. Res.* **49**(22), 11814–11824 (2010)